Medical Engineering & Physics 31 (2009) 1110–1117

Contents lists available at ScienceDirect

Medical Engineering & Physics

journal homepage: www.elsevier.com/locate/medengphy

Advanced modeling strategy for the analysis of heart valve leaflet tissue mechanics using high-order finite element method

Hadi Mohammadi [a,*], Fereshteh Bahramian [a,b], Wankei Wan [a]

[a] Biomedical Engineering Graduate Program, The University of Western Ontario, London, Ontario, Canada
[b] Department of Mechanical and Materials Engineering, The University of Western Ontario, London, Ontario, Canada

ARTICLE INFO

Article history:
Received 21 October 2008
Received in revised form 9 July 2009
Accepted 10 July 2009

Keywords:
Finite element method
High-order element
Bilinear material model
Anisotropy
Heart valve
Soft tissue

ABSTRACT

Modeling soft tissue using the finite element method is one of the most challenging areas in the field of biomechanical engineering. To date, many models have been developed to describe heart valve leaflet tissue mechanics, which are accurate to some extent. Nevertheless, there is no comprehensive method to modeling soft tissue mechanics, This is because (1) the degree of anisotropy in the heart valve leaflet changes layer by layer due to a variety of collagen fiber densities and orientations that cannot be taken into account in the model and also (2) a constitutive material model fully describing the mechanical properties of the leaflet structure is not available in the literature. In this framework, we develop a new high-order element using p-type finite element formulation to create anisotropic material properties similar to those of the heart valve leaflet tissue in only one single element. This element also takes the nonlinearity of the leaflet tissue into consideration using a bilinear material model. This new element is composed a two-dimensional finite element in the principal directions of leaflet tissue and a p-type finite element in the direction of thickness. The proposed element is easy to implement, much more efficient than standard elements available in commercial finite element packages. This study is one step towards the modeling of soft tissue mechanics using a meshless finite element approach to be applied in real-time haptic feedback of soft-tissue models in virtual reality simulation.

1. Introduction

Finite element analysis (FEA) has been extensively used for the structural analysis and functional simulation of heart valve (HV) leaflet tissue. Material models employed in previous studies for simulation of HV leaflet tissues such as porcine valves or pericardial bovine valves using the finite element method (FEM) can be generally categorized into four groups: linear isotropic [1–5], nonlinear isotropic [6–9], linear anisotropic [10–12] and nonlinear anisotropic [13] that come with varying degrees of accuracy. Lou and co-workers and Li and co-workers presented a nonlinear anisotropic model for porcine HV and analyzed the effect of geometry and nonlinearity of the tissue mechanical properties on stress distribution in a porcine HV [14,15]. De Hart et al. studied the effect of collagen fibers on mechanics and hemodynamics of a trileaflet aortic valve using numerical methods [16]. To simulate the effect of collagen remodeling on the mechanical properties of the aortic valve, a finite element model was used. In their study, collagen remodeling was assumed to be the net result of collagen synthesis and degradation. Recently Kim et al. has provided a new approach using a Fung-type elastic constitutive model for pericardial bioprosthetic HVs accounting for anisotropy and hyperelasticity of the HV leaflets [17]. In another study, we developed a new hybrid element to be used in heart valve leaflet tissue mechanics simulation, which can be applied to any other soft tissues. This novel element was a combination of hyperelastic isotropic elements and spar elements in the direction of collagen fibers. However, despite the effectiveness of this model, compared to the proposed approach, it was very time-consuming [19].

In this study, we design a new high-order anisotropic and bilinear element to be used in HV leaflet tissue mechanics simulation under physiological conditions. The specific advantage of the proposed element compared to other similar elements is that this element deals with less numerical complexities due to its independency on a strain energy density function, thus, it is quick. It also takes into consideration the realistic material properties. The FE formulation employed in this study is a combination of p-type and Galerkin FE. The proposed element is new and offers similar accuracy as the equivalent nonlinear FEM solution to the same model while solutions are obtained in a fraction of the CPU time.

* Corresponding author at: Graduate Program in Biomedical Engineering, The University of Western Ontario, London, Ontario N6A 5B9, Canada.
Tel.: +1 519 661 2111x81282; fax: +1 519 850 2308.
E-mail address: hmohamm3@uwo.ca (H. Mohammadi).

1350-4533/$ – see front matter. Crown Copyright © 2009 Published by Elsevier Ltd on behalf of IPEM. All rights reserved.
doi:10.1016/j.medengphy.2009.07.012

2. Method

HV leaflet is formed by stacking three layers with different mechanical properties, thus, considered a biocomposite layered thin plate. The theories available in the literature for such a composition are based on the equivalent single theory layer, including classical laminates theory and shear deformation laminates theory, and three-dimensional elasticity theory, including three-dimensional elasticity and layer wise theory (for more details see [19,20]).

The p-type FE to be used for the leaflet tissue mechanics is relatively new. The present study is based on a new three-dimensional high-order element that contains a two-dimensional high-order element in the "in-plane" domain and one-dimension polynomial in the direction of the thickness of the leaflet (the "out-of-plane" domain) using a p-type FE.

2.1. Geometry of the valve tissue

The leaflet geometry is developed based on the design procedure proposed in our other study using Bezier surfaces [18]. This geometry corresponds to that of porcine aortic HV leaflet geometry reported in [21]. The stent specifications and dimensions are listed in Table 1.

The geometry used for this study is shown in Fig. 1 consisting of three identical leaflets made of 55 control points as described in [18]. The thickness of the HV leaflet is not uniform and varies over a range of 0.1–1.4 mm [14]. In our model, we assume the leaflets are of uniform thickness (0.8 mm).

Table 1
Dimensions of the HV stent.

Valve size (outer diameter of the stent)	30.0 mm
Orifice diameter (inner diameter of the stent)	28.0 mm
Sewing ring diameter	35.0 mm
Valve height	17.5 mm
Aortic protrusion (valve height minus the height of saddle arc on sewing ring)	14.5 mm

Table 2
The stiffness values of the porcine aortic HV leaflet tissue in the two principal directions (circumferential and longitudinal).

	Strain	0–25%	25–60%
Young's modulus (E)	Circumferential	360 kPa	3.29 MPa
	Longitudinal	62 kPa	615 kPa

2.2. Material properties of the leaflet tissue

We measured the stress–strain curves of the porcine aortic valve in two principal directions, i.e., the radial and circumferential directions as shown in Fig. 2. The stress–stain curve can be considered a bilinear material model, which is soft in low strains (<25%) and stiff in high strains (>25%) (Fig. 2A). The bilinear stiffness of the HV leaflet tissue in the two principal directions (longitudinal and circumferential) is listed in Table 2. Since the stiffness in the circumferential direction is higher than the longitudinal direction, the shear modulus of elasticity G is calculated based on E_{Cir} as follows: $G = E_{Cir}/2(1+\upsilon)$, where G is the shear modulus of elasticity, E_{Cir} is

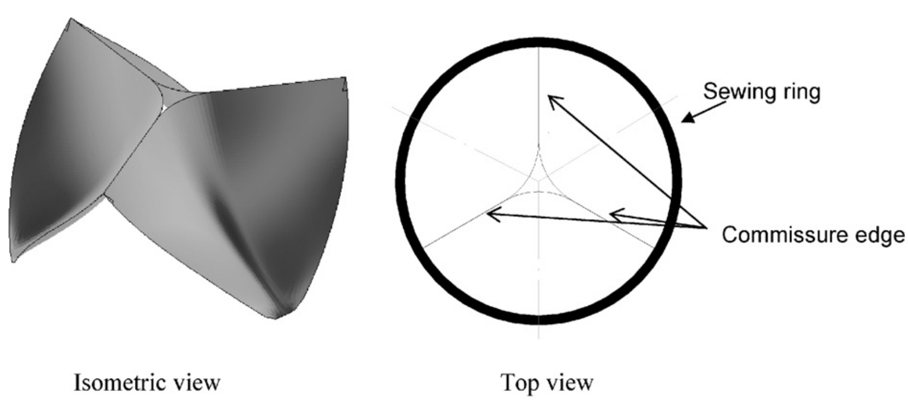

Fig. 1. The geometry of the HV leaflet tissue developed using Bezier type surfaces as described in [18].

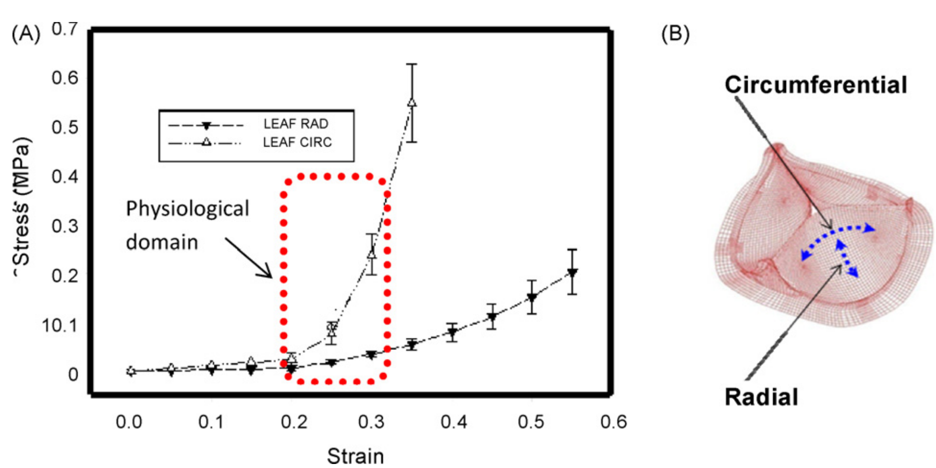

Fig. 2. The stress–strain curve for the porcine aortic HV leaflet tissue (A) in two principal directions as shown in (B). The radial direction in the figure corresponds to the longitudinal direction. It should be noted that the physiological range falls within the a strain between 20% and 30% [18].

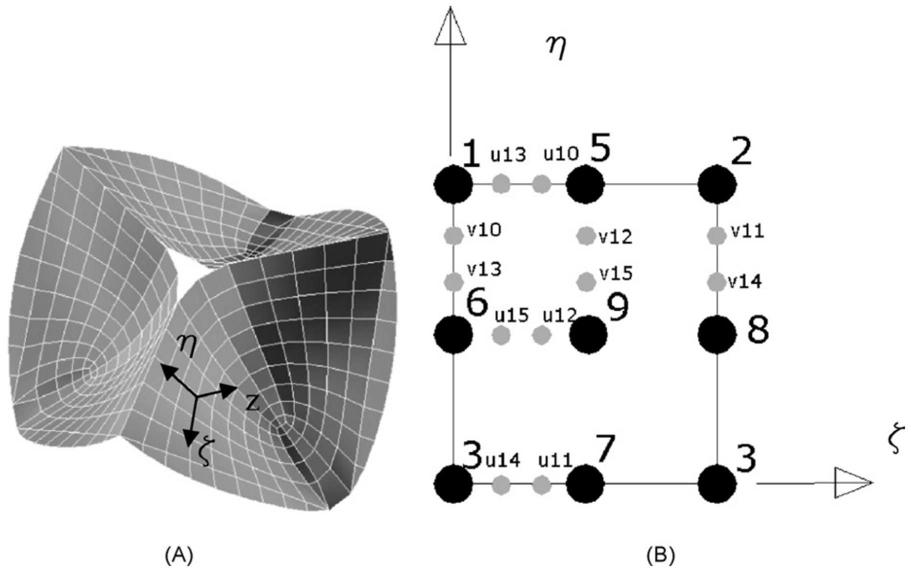

Fig. 3. The geometry of the HV leaflet tissue covered with only 183 high-order elements (A) and one single high-order element with demonstration of major and minor nodes (B).

the Young's modulus in the circumferential direction and υ is the Poisson's ratio assumed to be 0.45 [22].

2.3. The novel anisotropic high-order element

A new high-order element is proposed in this section. This element is nonlinear (bilinear) and anisotropic, possessing two principal directions, the circumferential direction and the longitudinal direction, as shown in Fig. 2B. The HV leaflet is made up of 183 high-order elements as shown in Fig. 3A. The schematic three-dimensional structure of the proposed high-order element is shown in Fig. 3B. This element consists of 20 nodes with nonlinear boundaries designed specifically for the HV leaflet. Each element is assigned a total degree of freedom (DOF) of 55, i.e., DOF = 15 for u components, DOF = 15 for v components and DOF = 25 for w components, where u, v and w are the principal displacement vector components in ζ, η and z directions, respectively at each node as shown in Fig. 3. The three-dimensional displacement field of the element is based on a two-dimensional high-order element extended in the direction of z, perpendicular to the $\zeta\eta$-plane, using a one-dimensional Lagrange interpolation function. The Lagrange function can be either linear, parabolic or cubic. The in-plane displacement field of the proposed high-order element is a combination of trigonometric and polynomial functions (for details see [18] and [19]). The displacement field is obtained by a tensor product of a two-dimensional high-order elements shape functions (SF) $N(\zeta, \eta)$ in $\zeta\eta$-plane along with a one-dimensional Lagrange interpolation function $N(z)$ in the direction of z. The displacement field for this element is defined as [19]:

$$u(\zeta, \eta, z) = \sum_{i=1}^{t} \left(\sum_{k=1}^{p} N_i^u(\zeta, \eta) \cdot u_{ik} \right) \cdot N_k(z) \tag{1}$$

$$v(\zeta, \eta, z) = \sum_{i=1}^{r} \left(\sum_{k=1}^{p} N_i^v(\zeta, \eta) \cdot v_{ik} \right) \cdot N_k(z) \tag{2}$$

$$w(\zeta, \eta, z) = \sum_{i=1}^{s} \left(\sum_{k=1}^{p} N_i^w(\zeta, \eta) \cdot w_{ik} \right) \cdot N_k(z) \tag{3}$$

where t, r and s are DOFs of the components of displacement vectors, i.e., u, v and w on each element, respectively. P is the order of the polynomial used for the Lagrange interpolation function in the direction of z, where $P = 2$, 3 and 4 for a linear, parabolic and cubic function, respectively, and u_{ik}, v_{ik} and w_{ik} are the components of the displacement vector at node ik. See Appendix A for more details.

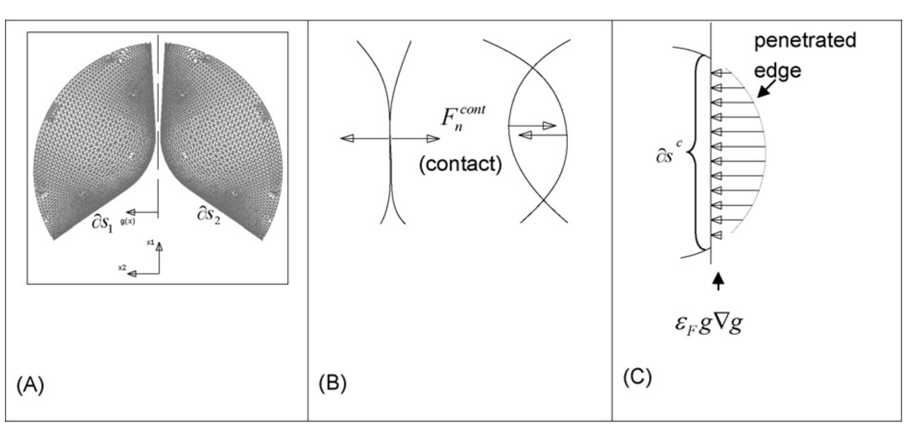

Fig. 4. (A) Geometry of the leaflets to be solved for a pushback contact solution, (B) surfaces before and after contact and (C) penalty method to contact force.

2.4. Leaflets contact

The contact surfaces and the corresponding force are determined by interactive computation of a pushback force which is calculated on nodes. To characterize the kinematics of the contact we define two symmetrical leaflets whose surfaces are ∂s_1 and ∂s_2 in a three-dimensional space shown in Fig. 4A/B. The distance from each point on the leaflet from the central plane is defined by a scalar function, $g(x)$, which is the "gap" function. Assuming frictionless contact, the contact force must be normal to the surface of the leaflets (Fig. 4A). The normal vector is a partial derivative of $g(x)$ with respect to the spatial coordinates. Thus the contact force is [23]:

$$F_n = P_r \frac{\partial g(x)}{\partial x} = P_r \nabla g \tag{4}$$

where P_r is the pressure. The penalty method replaces the contact force with the penalty $\varepsilon_{\mathrm{F}} g$ as shown in Fig. 4C, where ε_{F} is the penalty coefficient. As in FEM all forces must be discretized into nodal equivalent force, the contact force in the penalty formulation is discretized as follows [23]:

$$F_e^{cont} = \int_{\partial s^c} \varepsilon_{\mathrm{F}} g \nabla g N_e(x_1, x_2) da \tag{5}$$

where $\varepsilon_{\mathrm{F}} g \triangledown g$ is the contact penalty force, N_e is the shape function, ∂s^c is the contact area, da is the element area, and F_e^{cont} is the nodal equivalent contact force on node e.

2.5. Pressure follower force

Force vectors are defined in such a way that their directions always remain normal to the surface in the current configuration each time [24]. A shell element with an applied uniform pressure p_r on the current configuration which has a unit normal n, is considered. The traction force vector, t is expressed as $p_r n$ and the corresponding virtual external work in the current configuration is in the form:

$$\delta W^{ext} = \int_{\Gamma} \delta \Delta \cdot p_r n \; d\Gamma \tag{6}$$

where Δ is the displacement vector of the surface, n is the normal vector to the surface, p_r is the pressure and W^{ext} is the external work done by the pressure. A uniform aortic pressure of $p_r = 16$ kPa (120 mmHg) is assumed on the top surface of the leaflet.

3. Results

3.1. Stress distribution on the leaflet

Two models are considered: (1) A single leaflet is modeled without taking into consideration the effect of contact that occurs between the two adjacent leaflets in the closing phase (Fig. 5) and (2) the complete valve with three leaflets is modeled accounting for the contact and its effect on mechanical performance of the valve (Fig. 6). For each model, we assume that the leaflet is composed of two distinct layers on top of each other. The top layer corresponds to fibrosa (the layer of the leaflet facing the aorta) and the bottom layer corresponds to ventricularis (the layer of the leaflet facing the left ventricle).

Fig. 5 shows the distribution of the maximum principal stresses over the two layers applied on a single leaflet tissue (model I). Results show that the values of principal stresses are slightly different in the top and bottom layers. The maximum of the first principal stresses (the maximum principal stress) are 580 kPa and 602 kPa in the top and bottom layers, respectively. Also, in this model, as shown in Fig. 5A, the maximum principal stress is located lower

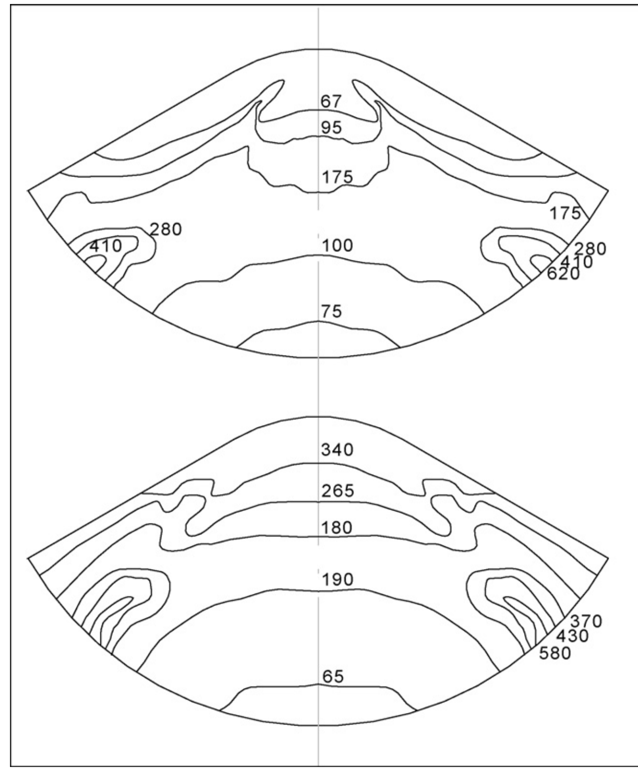

Fig. 5. The maximum principal stresses distribution over the leaflet tissue on the top layer (A) and on the bottom layer (B), with no contact considered between the two adjacent leaflets—values are in kPa.

than the corners of the leaflets on the attachment of the leaflets to the stent. Li et al. reported similar locations and values for high principal stress regions in porcine HV leaflets using a transversely isotropic material model in a FE model [14]. We also did a similar study on the HV leaflet tissue with a different material model as described in [18]. The proposed element offers similar accuracy (with <5% error) as the equivalent nonlinear FEM solutions detailed

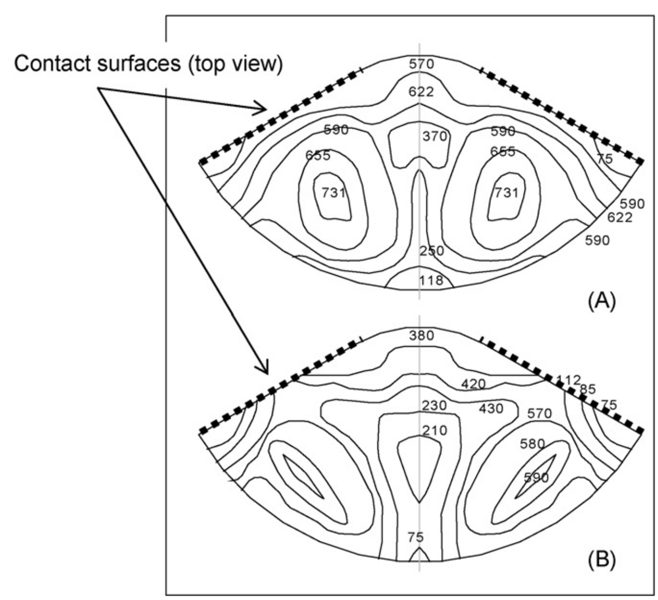

Fig. 6. The maximum principal stresses distribution over the leaflet tissue on the top layer (A) and on the bottom layer (B), accounting for the contact between the two adjacent leaflets—values are in kPa.

in [14] and [18] while solutions are obtained in a fraction of the CPU time.

In model II, contact between the two adjacent leaflets is considered. Results show that the coaptation area has a direct effect on the maximum principal stresses. The maximum principal stresses over the leaflet for the two layers of the leaflet tissue are shown in Fig. 6. The maximum values for the first principal stress (max. principal stress) on the top and bottom layers are slightly higher compared to model I (no contact). The maximum values are 731 kPa for the top layer and 590 kPa for the bottom layer. Also, the location of the maximum principal stress in model II (with contact) is not the same as when contact is not taken into consideration. In fact, the location with maximum values of stress is not on the attachment, but is located on the center of the leaflet, slightly away from the attachment, as shown in Fig. 6.

In Li's model, contact has not been taken into consideration and thus, the results obtained by their model cannot be realistic. In other words, their results cannot show the same values as experienced by a normal valve leaflet under physiological conditions. Our results show that with taking the effect of contact into account the values of principal stresses increase by ∼10%. Recently Kim et al. has provided a new approach using a Fung-type elastic constitutive model for pericardial bioprosthetic HVs accounting for anisotropy and hyperelasticity of the HV leaflets [17]. They did not model the contact, as this feature is not available for hyperelastic elements in FE commercial packages. Fig. 6 clearly shows that the contact between the leaflets has a significant effect on the stress distribution both in location and values. Based on our results the crucial locations are close to, but not exactly on, the stent attachments, as shown in Fig. 7A and B with a maximum values of 621 kPa on the top layer and 667 kPa on the bottom layer.

Fig. 7 shows the bending moment per unit length (M) for model II, which is calculated by knowing the values of stresses in the top and bottom layers, as such:

$$M = \sqrt{M_x^2 + M_y^2 - M_x M_y + 3M_{xy}^2} \tag{6}$$

$$M_x = (\sigma_x^{top} - \sigma_x^{bottom})\frac{h^2}{12} \tag{7}$$

$$M_y = (\sigma_y^{top} - \sigma_y^{bottom})\frac{h^2}{12} \tag{8}$$

$$M_{xy} = (\tau_{xy}^{top} - \tau_{xy}^{bottom})\frac{h^2}{12} \tag{9}$$

where x and y are the circumferential and longitudinal directions, respectively. Results indicate that the bending moment is maximum in the vicinity of the contact area with a value of 12.7 mN. Maximum bending deformation also occurs in the same area. Bending moment is consistently low in the areas close to the attachment, however, in these areas the values of principal stress are maximum.

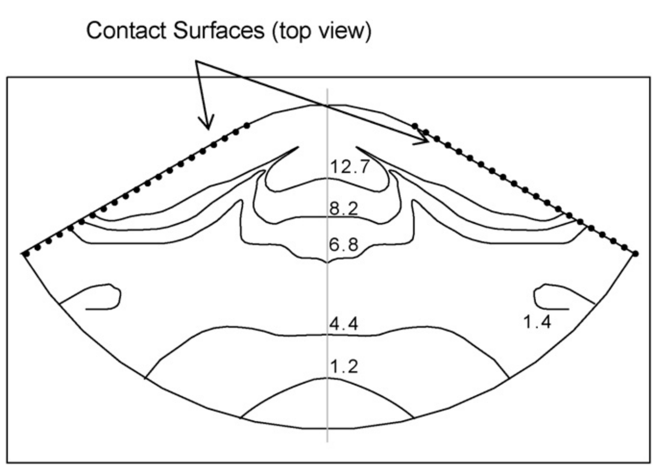

Fig. 7. The bending moment per unit length (mN)—in the vicinity of the contact area bending moment is maximum.

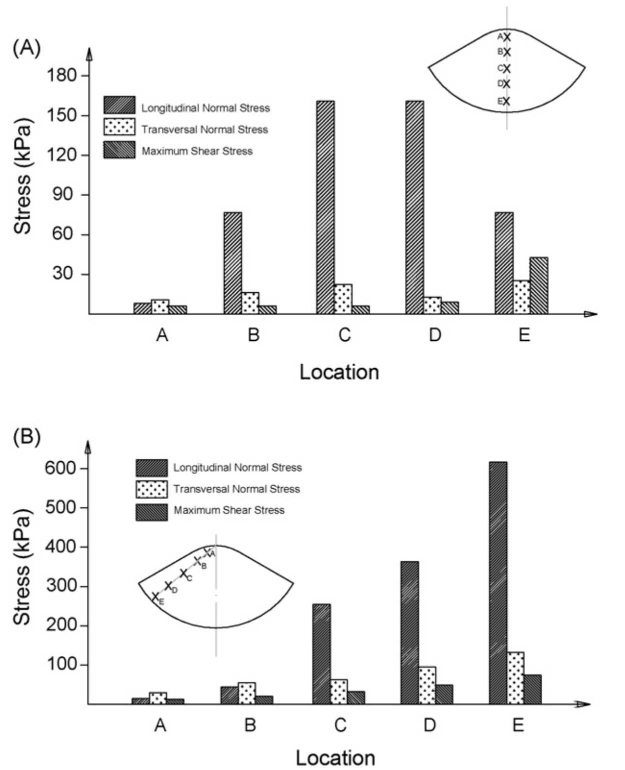

Fig. 8. Longitudinal normal stress, transversal normal stress and the maximum shear stress with respect to labeled locations, (A) on the midline of the leaflet, (B) on the line passing over the maximum values.

Li et al. reported that the maximum bending moment per unit length is close to the coaptation area with a value of 11.2 mN. Also, distribution of the bending moment calculated for the closing phase is in good agreement to ones of Li's model (less then 5% error) [14]. Fig. 8 shows values of stress including in-plane stress (max. shear stress) and out-of-plane stresses (longitudinal and transversal normal stresses) with respect to labeled locations. The direction shown in Fig. 8A is the midline of the leaflet or the axis of symmetry and Fig. 8B shows the path where maximum values of stress occur. As shown in Fig. 8, the critical values of stress do not occur at the midline where the maximum deformation occur, however, longitudinal normal stress, transversal normal stress and maximum shear stress are maximum in the area close to the corners on the attachment of the leaflet to the stent.

3.2. Deformation of the leaflets

Results indicate that the surface area is initially 6.07 cm^2 and is 6.68 cm^2 after deformation without considering the effect of contact and 6.42 cm^2 when accounting for the contact, as shown in Fig. 9. This corresponds to 10% and 5.29% area expansion, respectively. Results also show two long wrinkles in the middle of the leaflet close to the symmetry line, which is due to the coaptation area (Fig. 9). The smaller the orifice area is, the smaller the wrinkle zone (data are not presented). As shown in Fig. 9, the wrinkles are symmetric as the pressure applied on the leaflets are assumed to be uniform and symmetric. However, neither aortic pressure nor ventricular pressure is constant and uniform as they are both time and location dependent, thus, wrinkles may be formed irregularly in

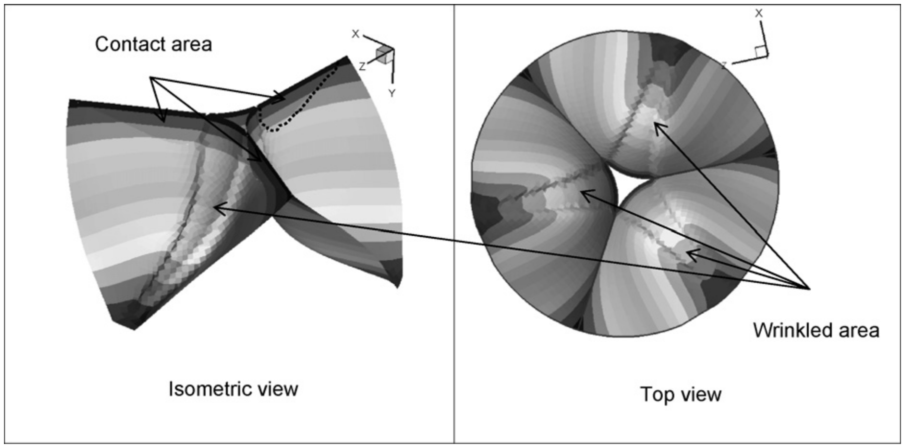

Fig. 9. Deformation of the HV leaflet in the closing phase. The contact area and the wrinkled area after deformation due to contact are shown with arrows.

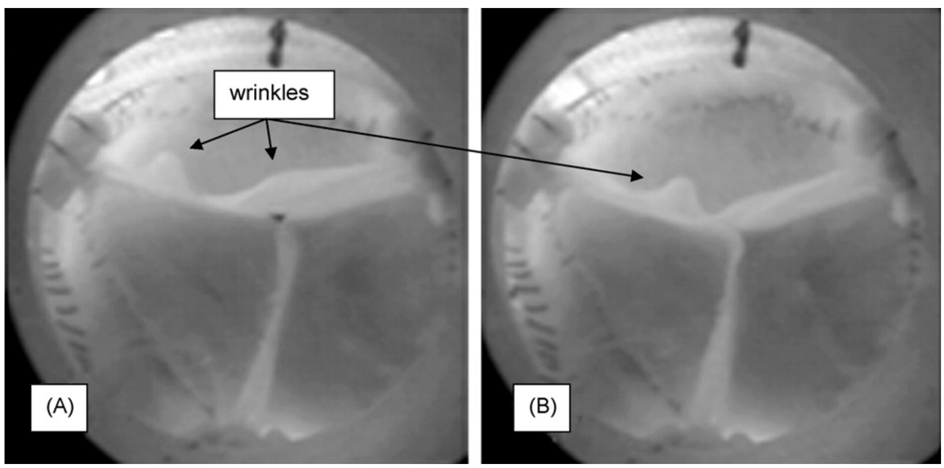

Fig. 10. The closing phase in a normal aortic heart valve function. The contact area and the wrinkled area after deformation are shown with arrows. (A) and (B) are showing different locations for wrinkle to from during the closing phase at different cycles.

Table 3
A comparison between the performance of the approach proposed in this study versus the other conventional approach.

Model	Max. principal stress	Max. normalized bending moment	Contact	CPU time
Hybrid element [18]	636 kPa	10.5 mN	Available	>30 min[a]
High-order element (in this study)	622 kPa	12.7 mN	Available	<12 s[b]
Li et al. [14]	580 kPa	11.7 mN	Not available	NA[c]

[a] 8 parallel processors each @ 1.44 GHz, 0.99 GB of RAM.
[b] Processor used: @ 1.60 GHz, 0.99 GB of RAM.
[c] Not available.

various locations depending on the pressure variety and the thickness of the valve as thickness plays a major role in the length and depth of wrinkles. Experimental observations approve the presence of irregular wrinkles around the midline of the leaflet in the closing phase [25] as shown in Fig. 10. Using the proposed high-order element in this study, wrinkles can be simulated and analyzed. This is novel and reported for the first time using a FE model and clearly shows the capability of the proposed element in modeling of wrinkle using high-order FE. Table 3 outlines the CPU time, the maximum principle stresses, the maximum normalized bending moment and the capability of the approach used for modeling contact for the high-order element proposed in this study and for other conventional approach using hyperelastic material models [14,18].

The proposed element is new and offers similar accuracy as the equivalent nonlinear FEM solution to the same model. In a hyperelastic material model implemented in [18], although eight parallel processors were used, but the computational time for the stress analysis of the heart valve leaflet (consist of ~11,000 elements) is always more than 30 min. The high-order element proposed in this study which uses only one processor at 1.60 GHz and 1.00 GB of RAM solves the same model is less than 12 s.

4. Conclusion

A new high-order element, which is anisotropic and bilinear, has been developed to mechanically analyze a trileaflet natural aortic HV. Stress pattern, maximum principal stresses, distribution of bending moments, the contact area between to adjacent leaflets and in-plane and out-of plane stresses in closing phase have been calculated. The proposed element deals with less complexities thus is much faster than the equivalent nonlinear finite element. The technique has similar accuracy to the equivalent nonlinear FEM solution using the model while solutions are obtained in a fraction of the CPU time. However, defining a strain energy density function for soft tissues is generally quite difficult, if not impossible. This element can be easily developed to possess any degree of anisotropy using a bilinear material model.

There are some limitations with the FE model. Firstly, in the FE analysis the leaflets were subjected to a uniform pressure load on the aortic side during the valve closing phase. Fluid flow patterns may vary in different regions, particularly in the vicinity of the valve leaflets. Hence, spatially non-uniform pressure and shear stress distributions can be induced on the surface of the leaflets during the opening and closing phases, affecting the consequent deformation of the leaflets. A more realistic analysis of the fluid-induced stresses on aortic leaflet tissue will require a comprehensive fluid structure interaction model. Secondly, the material parameters of the employed material model were assumed to be homogeneous through the entire leaflet, i.e., the material modeling of a complete leaflet was defined by one set of the material parameters along with the assumption of a constant leaflet thickness. Lastly, the overall displacements of the valve motion and the stress distributions on the valve leaflets from the three-dimensional dynamic FE simulations reported in this work were qualitatively compared with previous studies. Quantitative validation of the leaflet deformation in the dynamic analysis will require the material property data from the biaxial tests for each leaflet of a particular valve. This must be followed by the comparison of the predicted local strain distribution on the leaflets with experimentally measured strain fields from the same valve tested under dynamic loading.

Conflict of interest

The authors declare that they have no proprietary, financial, professional or other personal interests of any nature or kind that could be construed as influencing the position presented in this article.

Acknowledgment

The authors would like to thank the Canadian Institute of Health Research (CIHR) for the financial support.

Appendix A. The in-plane displacement field including trigonometric and polynomial functions are defined as follows:

$$u = \sum_{i=1}^{9} N_i^u u_i + \sin(2\pi\zeta)\begin{Bmatrix} L_1(\eta) \\ L_2(\eta) \\ L_3(\eta) \end{Bmatrix}^T \begin{Bmatrix} u_{10} \\ u_{11} \\ u_{12} \end{Bmatrix} + \sin(4\pi\zeta)\begin{Bmatrix} L_1(\eta) \\ L_2(\eta) \\ L_3(\eta) \end{Bmatrix}^T \begin{Bmatrix} u_{13} \\ u_{14} \\ u_{15} \end{Bmatrix} \tag{A1}$$

$$v = \sum_{i=1}^{9} N_i^v v_i + \sin(2\pi\zeta)\begin{Bmatrix} L_1(\eta) \\ L_2(\eta) \\ L_3(\eta) \end{Bmatrix}^T \begin{Bmatrix} v_{10} \\ v_{11} \\ v_{12} \end{Bmatrix} + \sin(4\pi\zeta)\begin{Bmatrix} L_1(\eta) \\ L_2(\eta) \\ L_3(\eta) \end{Bmatrix}^T \begin{Bmatrix} v_{13} \\ v_{14} \\ v_{15} \end{Bmatrix} \tag{A2}$$

$$w = \sum_{i=1}^{16} N_j^w \psi_j + \phi(\zeta)\begin{Bmatrix} H_1(\eta) \\ H_2(\eta) \\ H_3(\eta) \\ H_4(\eta) \end{Bmatrix}^T \begin{Bmatrix} w_5 \\ w_{y5} \\ w_7 \\ w_{y7} \end{Bmatrix} + \phi(\eta)\begin{Bmatrix} H_1(\zeta) \\ H_2(\zeta) \\ H_3(\zeta) \\ H_4(\zeta) \end{Bmatrix}^T \begin{Bmatrix} w_8 \\ w_{x8} \\ w_6 \\ w_{x6} \end{Bmatrix} + \phi(\eta)\phi(\zeta)w_9 \tag{A3}$$

where u are v are in-plane displacements and w is the displacement in direction of thickness (z). L_i's and H_i's are Lagrange and Hermit polynomials. ϕ and ψ are the first modal shape of the clamped beam and out-of-plane bending vibrations at the center node of the high-order element, respectively. u_{10}, u_{11}, u_{12}, u_{13}, u_{14}, and u_{15} and v_{10}, v_{11}, v_{12}, v_{13}, v_{14}, and v_{15} are amplitude of the sign functions of the model. Sinusoidal terms are used to model the nonlinear in-plane geometric effects. The quadratic Lagrange polynomials take the form of:

$$\begin{aligned} L_1(\zeta) &= 2\zeta^2 - 3\zeta + 1 \\ L_2(\zeta) &= 2\zeta^2 - \zeta \\ L_3(\zeta) &= 4(\zeta - \zeta^2) \end{aligned} \tag{A4}$$

The Hermitian polynomials take the form of:

$$\begin{aligned} H_1(\zeta) &= 1 - 3\zeta^2 - 2\zeta^3 \\ H_2(\zeta) &= a(\zeta - 2\zeta^2 + \zeta^3) \\ H_3(\zeta) &= 3\zeta^2 - 2\zeta^3 \\ H_4(\zeta) &= a(-\zeta^2 + \zeta^3) \end{aligned} \tag{A5}$$

The SF for the in-plane displacement field, i.e., N_i^u, N_i^v and N_i^w are defined as follows:

$$\begin{array}{lll} N_1^u = L_1(\zeta)L_2(\zeta) & N_2^u = L_2(\zeta)L_1(\zeta) & N_3^u = L_2(\zeta)L_2(\zeta) \\ N_4^u = L_1(\zeta)L_2(\zeta) & N_5^u = L_3(\zeta)L_1(\zeta) & N_6^u = L_2(\zeta)L_3(\zeta) \\ N_7^u = L_3(\zeta)L_2(\zeta) & N_8^u = L_1(\zeta)L_3(\zeta) & N_9^u = L_3(\zeta)L_3(\zeta) \\ N_{10}^u = \sin(2\pi\zeta)L_1(\eta) & N_{11}^u = \sin(2\pi\zeta)L_2(\eta) & N_{12}^u = \sin(2\pi\zeta)L_3(\eta) \\ N_{13}^u = \sin(4\pi\zeta)L_1(\eta) & N_{14}^u = \sin(4\pi\zeta)L_2(\eta) & N_{15}^u = \sin(4\pi\zeta)L_3(\eta) \end{array} \tag{A6}$$

For $N_i^v = N_i^u$ for $i \le 9$ and the rest of SFs for the v component are

$$\begin{array}{lll} N_{10}^v = \sin(2\pi\eta)L_1(\eta) & N_{11}^v = \sin(2\pi\eta)L_2(\eta) & N_{12}^v = \sin(2\pi\eta)L_3(\eta) \\ N_{13}^v = \sin(4\pi\eta)L_1(\eta) & N_{14}^v = \sin(4\pi\eta)L_2(\eta) & N_{15}^v = \sin(4\pi\eta)L_3(\eta) \end{array} \tag{A7}$$

and the SFs in the direction of z are

$$\begin{array}{lll} N_1^w = H_1(\zeta)H_1(\eta) & N_2^w = H_2(\zeta)H_1(\eta) & N_3^w = H_1(\zeta)H_2(\eta) \\ N_4^w = H_2(\zeta)H_2(\eta) & N_5^w = H_3(\zeta)H_1(\eta) & N_6^w = H_4(\zeta)H_1(\eta) \\ N_7^w = H_3(\zeta)H_2(\eta) & N_8^w = H_4(\zeta)H_2(\eta) & N_9^w = H_3(\zeta)H_3(\eta) \\ N_{10}^w = H_4(\zeta)H_3(\eta) & N_{11}^w = H_3(\zeta)H_4(\eta) & N_{12}^w = H(\zeta)H_4(\eta) \\ N_{13}^w = H_1(\zeta)H_3(\eta) & N_{14}^w = H_2(\zeta)H_3(\eta) & N_{15}^w = H_1(\zeta)H_4(\eta) \\ N_{16}^w = H_2(\zeta)H_4(\eta) & N_{17}^w = \phi(\zeta)H_1(\eta) & N_{18}^w = \phi(\zeta)H_2(\eta) \\ N_{19}^w = \phi(\eta)H_3(\zeta) & N_{20}^w = H_4(\zeta)\phi(\eta) & N_{21}^w = H_3(\zeta)\phi(\zeta) \\ N_{22}^w = H_4(\zeta)\phi(\zeta) & N_{23}^w = H_1(\zeta)\phi(\eta) & N_{24}^w = H_2(\zeta)\phi(\eta) \end{array} \tag{A8}$$

and for N_{25}^w, we will define: $N_{25}^w = \phi(\zeta)\phi(\eta)$

A cubic Lagrange interpolation function ($N_k(z)$) can be written in the form of (for the case $P=4$) [2]:

$$\begin{aligned}
N_1(z) &= \frac{9}{2t^3}\left(z-\frac{t}{6}\right)\left(z+\frac{t}{6}\right)\left(z+\frac{t}{2}\right)\\
N_2(z) &= \frac{27}{2t^3}\left(z-\frac{t}{2}\right)\left(z-\frac{t}{6}\right)\left(z+\frac{t}{2}\right)\\
N_3(z) &= \frac{27}{2t^3}\left(z-\frac{t}{2}\right)\left(z+\frac{t}{6}\right)\left(z+\frac{t}{2}\right)\\
N_4(z) &= \frac{9}{2t^3}\left(z-\frac{t}{2}\right)\left(z+\frac{t}{2}\right)\left(2+\frac{t}{2}\right)
\end{aligned} \tag{A9}$$

where t is the thickness of the leaflet.

The proposed high-order element offers a complete three-dimensional state of stress and strain. A standard Galerkin FE is used to describe the stiffness matrix [K] and the mass matrix [m] as more details can be found in [20].

References

[1] Cataloglu A, Clark RE, Gould PL. Stress analysis of aortic valve leaflets with smoothed geometrical data. Journal of Biomechanics 1977;10(3):153–8.
[2] Chandran KB, Kim SH, Han G. Stress distribution on the cusps of a polyurethane trileaflet HV prosthesis in the closed position. Journal of Biomechanics 1991;24(6):385–95.
[3] Ghista DN, Reul H. Optimal prosthetic aortic leaflet valve: design parametric and longevity analyses: development of the Avcothane-51 leaflet valve based on the optimum design analysis. Journal of Biomechanics 1977;10(5–6):313–24.
[4] Hamid MS, Sabbah HN, Stein PD. Influence of stent height upon stresses on the cusps of closed bioprosthetic valves. Journal of Biomechanics 1986;19(9):759–69.
[5] Rousseau EP, van Steenhoven AA, Janssen JD. A mechanical analysis of the closed hancock heart valve prosthesis. Journal of Biomechanics 1988;21(7):545–62.
[6] Black MM, Howard IC, Huang X, Patterson EA. A three-dimensional analysis of a bioprosthetic heart valve. Journal of Biomechanics 1991;24(9):793–801.
[7] Howard IC, Patterson EA, Yoxall A. On the opening mechanism of the aortic valve: some observations from simulations. Journal of Medical Engineering Technology 2003;27(6):259–66.
[8] Huang X, Black MM, Howard IC, Patterson EA. A two-dimensional finite element analysis of a bioprosthetic heart valve. Journal of Biomechanics 1990;23(8):753–62.
[9] Patterson EA, Howard IC, Thornton MA. A comparative study of linear and nonlinear simulations of the leaflets in a bioprosthetic heart valve during the cardiac cycle. Journal of Medical Engineering Technology 1996;20(3): 95–108.
[10] Grande KJ, Cochran RP, Reinhall PG, Kunzelman KS. Stress variations in the human aortic root and valve: the role of anatomic asymmetry. Annual Journal of Biomedical Engineering 1998;26(4):534–45.
[11] Grande KJ, Cochran RP, Reinhall PG, Kunzelman KS. Mechanisms of aortic valve incompetence in aging: a finite element model. Journal of Heart Valve Disease 1999;8(2):149–56.
[12] Grande KJ, Cochran RP, Reinhall PG, Kunzelman KS. Mechanisms of aortic valve incompetence: finite element modeling of aortic root dilatation. Annual Thoracic Surgery 2000;69(6):1851–7.
[13] Sun W, Abad A, Sacks MS. Simulated bioprosthetic heart valve deformation under quasi-static loading. ASME Journal of Biomechanical Engineering 2005;127(6):905–14.
[14] Li J, Lou XY, Kuang ZB. A nonlinear anisotropic model for porcine heart valves. Journal of Biomechanics 2001;34:1279–89.
[15] Luo XY, Li WG, Li J. Geometrical stress reduction factors in anisotropic porcine heart valves. Journal of Biomechanical Engineering 2003;125:735–44.
[16] De Hart, Peters GWM, Schreurs PGJ. Collagen fibers reduce stresses and stabilize motion of aortic valve leaflets during systole. Journal of Biomechanics 2004;37:303–11.
[17] Kim H, Jia L, Sacks MS, Chandran CB. Dynamic simulation precardial bioprosthetic valve function. Journal of Biomechanical Engineering 2006;128: 717–27.
[18] Mohammadi H, Boughner D, Millon LE, Wan WK. Design and simulation of a poly(vinyl alcohol)-bacterial cellulose nanocomposite mechanical aortic heart valve prosthesis, Proceedings of the Institution of Mechanical Engineers. Part H: Journal of Engineering in Medicine 2009;223:697–711.
[19] Koko TS, Olson D. Nonlinear analysis of stiffened plate using super element. Journal of Numerical Methods in Engineering 1991;31:149–67.
[20] Chapelle D, Bathe KJ. The finite element analysis of shells—fundamentals, computational fluid and solid mechanics. Springer; 2003.
[21] Hamid MS, Sabbah HN, Stein PD. Influence of stent height upon stresses on the cusps of closed bioprosthetic valves. Journal of Biomechanics 1986;19: 759–69.
[22] Vesely I, Noseworthy R. Micromechanics of the fibrosa and the ventricularis in aortic valve leaflets. Journal of Biomechanics 1992;25:101–13.
[23] Gerald F. Curves and surfaces for computer aided geometric design: a practical guide. Boston; Toronto: Academic Press; 1993.
[24] Mohammadi H, Bahramian F. A continuum model on reduction of numerical errors of finite element analysis in soft tissues modeling, the communications in numerical methods in engineering, in press. Ref # CNM-Mar-09-0081.
[25] Kollara A, Hartyanszky I. External subcommissural annuloplasty to prevent regurgitation in the pulmonary autograft. Interactive Cardiovascular and Thoracic Surgery 2003;2:183–5.